

# Journal of Astronomical Telescopes, Instruments, and Systems

AstronomicalTelescopes.SPIEDigitalLibrary.org

## In-orbit performance and calibration of the Hard X-ray Imager onboard Hitomi (ASTRO-H)

Kouichi Hagino  
Kazuhiro Nakazawa  
Goro Sato  
Motohide Kokubun  
Teruaki Enoto  
Yasushi Fukazawa  
Katsuhiro Hayashi  
Jun Kataoka  
Junichiro Katsuta  
Shogo B. Kobayashi  
Philippe Laurent  
Francois Lebrun  
Olivier Limousin  
Daniel Maier

Kazuo Makishima  
Taketo Mimura  
Katsuma Miyake  
Tsunefumi Mizuno  
Kunishiro Mori  
Hiroaki Murakami  
Takeshi Nakamori  
Toshio Nakano  
Hirofumi Noda  
Hirokazu Odaka  
Masanori Ohno  
Masayuki Ohta  
Shinya Saito  
Rie Sato

Hiroyasu Tajima  
Hiromitsu Takahashi  
Tadayuki Takahashi  
Shin'ichiro Takeda  
Takaaki Tanaka  
Yukikatsu Terada  
Hideki Uchiyama  
Yasunobu Uchiyama  
Shin Watanabe  
Kazutaka Yamaoka  
Yoichi Yatsu  
Takayuki Yuasa  
the HXI Team

Kouichi Hagino, Kazuhiro Nakazawa, Goro Sato, Motohide Kokubun, Teruaki Enoto, Yasushi Fukazawa, Katsuhiro Hayashi, Jun Kataoka, Junichiro Katsuta, Shogo B. Kobayashi, Philippe Laurent, Francois Lebrun, Olivier Limousin, Daniel Maier, Kazuo Makishima, Taketo Mimura, Katsuma Miyake, Tsunefumi Mizuno, Kunishiro Mori, Hiroaki Murakami, Takeshi Nakamori, Toshio Nakano, Hirofumi Noda, Hirokazu Odaka, Masanori Ohno, Masayuki Ohta, Shinya Saito, Rie Sato, Hiroyasu Tajima, Hiromitsu Takahashi, Tadayuki Takahashi, Shin'ichiro Takeda, Takaaki Tanaka, Yukikatsu Terada, Hideki Uchiyama, Yasunobu Uchiyama, Shin Watanabe, Kazutaka Yamaoka, Yoichi Yatsu, Takayuki Yuasa, the HXI Team "In-orbit performance and calibration of the Hard X-ray Imager onboard Hitomi (ASTRO-H)," *J. Astron. Telesc. Instrum. Syst.* 4(2), 021409 (2018), doi: 10.1117/1.JATIS.4.2.021409.

# In-orbit performance and calibration of the Hard X-ray Imager onboard Hitomi (ASTRO-H)

Kouichi Hagino,<sup>a,\*</sup> Kazuhiro Nakazawa,<sup>b,c</sup> Goro Sato,<sup>d</sup> Motohide Kokubun,<sup>d</sup> Teruaki Enoto,<sup>e,f</sup> Yasushi Fukazawa,<sup>g</sup> Katsuhiro Hayashi,<sup>d,h</sup> Jun Kataoka,<sup>i</sup> Junichiro Katsuta,<sup>g</sup> Shogo B. Kobayashi,<sup>j</sup> Philippe Laurent,<sup>k,l</sup> Francois Lebrun,<sup>k</sup> Olivier Limousin,<sup>l</sup> Daniel Maier,<sup>l</sup> Kazuo Makishima,<sup>m</sup> Taketo Mimura,<sup>i</sup> Katsuma Miyake,<sup>b</sup> Tsunefumi Mizuno,<sup>g,n</sup> Kunishiro Mori,<sup>d</sup> Hiroaki Murakami,<sup>b</sup> Takeshi Nakamori,<sup>o</sup> Toshio Nakano,<sup>p</sup> Hirofumi Noda,<sup>q,r</sup> Hirokazu Odaka,<sup>s</sup> Masanori Ohno,<sup>f</sup> Masayuki Ohta,<sup>d</sup> Shinya Saito,<sup>t</sup> Rie Sato,<sup>d</sup> Hiroyasu Tajima,<sup>u</sup> Hiromitsu Takahashi,<sup>g</sup> Tadayuki Takahashi,<sup>d</sup> Shin'ichiro Takeda,<sup>v</sup> Takaaki Tanaka,<sup>i</sup> Yukikatsu Terada,<sup>w</sup> Hideki Uchiyama,<sup>x</sup> Yasunobu Uchiyama,<sup>t</sup> Shin Watanabe,<sup>d</sup> Kazutaka Yamaoka,<sup>h,u</sup> Yoichi Yatsu,<sup>y</sup> Takayuki Yuasa,<sup>m</sup> and the HXI Team

<sup>a</sup>Tokyo University of Science, Department of Physics, Noda, Chiba, Japan

<sup>b</sup>The University of Tokyo, Department of Physics, Tokyo, Japan

<sup>c</sup>The University of Tokyo, Research Center for the Early Universe, School of Science, Tokyo, Japan

<sup>d</sup>Japan Aerospace Exploration Agency, Institute of Space and Astronautical Science, Sagamihara, Kanagawa, Japan

<sup>e</sup>Kyoto University, Department of Astronomy, Kyoto, Japan

<sup>f</sup>Kyoto University, The Hakubi Center for Advanced Research, Kyoto, Japan

<sup>g</sup>Hiroshima University, School of Science, Higashihiroshima, Japan

<sup>h</sup>Nagoya University, Department of Physics, Nagoya, Aichi, Japan

<sup>i</sup>Waseda University, Research Institute for Science and Engineering, Shinjuku, Tokyo, Japan

<sup>j</sup>Kyoto University, Department of Physics, Kyoto, Japan

<sup>k</sup>Laboratoire APC, Paris, France

<sup>l</sup>CEA Saclay, Gif sur Yvette, France

<sup>m</sup>Institute of Physical and Chemical Research, Wako, Saitama, Japan

<sup>n</sup>Hiroshima University, Hiroshima Astrophysical Science Center, Higashihiroshima, Hiroshima, Japan

<sup>o</sup>Yamagata University, Faculty of Science, Yamagata, Japan

<sup>p</sup>RIKEN Nishina Center, Wako, Saitama, Japan

<sup>q</sup>Tohoku University, Frontier Research Institute for Interdisciplinary Sciences, Sendai, Miyagi, Japan

<sup>r</sup>Tohoku University, Astronomical Institute, Sendai, Miyagi, Japan

<sup>s</sup>Stanford University, Kavli Institute for Particle Astrophysics and Cosmology, Stanford, California, United States

<sup>t</sup>Rikkyo University, Department of Physics, Tokyo, Japan

<sup>u</sup>Nagoya University, Institute for Space-Earth Environmental Research, Nagoya, Aichi, Japan

<sup>v</sup>Okinawa Institute of Science and Technology Graduate University, Onna-son, Okinawa, Japan

<sup>w</sup>Saitama University, Department of Physics, Saitama, Japan

<sup>x</sup>Shizuoka University, Faculty of Education, Shizuoka, Japan

<sup>y</sup>Tokyo Institute of Technology, Department of Physics, Tokyo, Japan

**Abstract.** The Hard X-ray Imager (HXI) onboard Hitomi (ASTRO-H) is an imaging spectrometer covering hard x-ray energies of 5 to 80 keV. Combined with the Hard X-ray Telescope, it enables imaging spectroscopy with an angular resolution of  $1'.7$  half-power diameter, in a field of view of  $9' \times 9'$ . The main imager is composed of four layers of Si detectors and one layer of CdTe detector, stacked to cover a wide energy band up to 80 keV, surrounded by an active shield made of  $\text{Bi}_4\text{Ge}_3\text{O}_{12}$  scintillator to reduce the background. The HXI started observations 12 days before the Hitomi loss and successfully obtained data from G21.5–0.9, Crab, and blank sky. Utilizing these data, we calibrate the detector response and study properties of in-orbit background. The observed Crab spectra agree well with a powerlaw model convolved with the detector response, within 5% accuracy. We find that albedo electrons in specified orbit strongly affect the background of the Si top layer and establish a screening method to reduce it. The background level over the full field of view after all the processing and screening is as low as the preflight requirement of  $1 - 3 \times 10^{-4}$  counts  $\text{s}^{-1} \text{cm}^{-2} \text{keV}^{-1}$ . © The Authors. Published by SPIE under a Creative Commons Attribution 3.0 Unported License. Distribution or reproduction of this work in whole or in part requires full attribution of the original publication, including its DOI. [DOI: [10.1117/1.JATIS.4.2.021409](https://doi.org/10.1117/1.JATIS.4.2.021409)]

Keywords: astronomy; satellites; x-rays; semiconductors; spectroscopy; imaging.

Paper 17059SS received Aug. 7, 2017; accepted for publication Mar. 9, 2018; published online Mar. 30, 2018.

## 1 Introduction

An international x-ray satellite, Hitomi, led by Japan was launched on February 17, 2016, by an H-IIA rocket at the Tanegashima Space Center in Japan and placed in a low-Earth orbit with an altitude of 575 km and an inclination angle of

31 deg.<sup>1</sup> Hitomi carries four types of instruments covering a wide energy range from soft x-ray to soft gamma ray. The hard x-ray imaging system composed of two sets of the Hard X-ray Imagers (HXI)<sup>2</sup> and two sets of the Hard X-ray Telescopes (HXT)<sup>3</sup> is capable of imaging spectroscopy in the hard x-ray band ranging from 5 to 80 keV.<sup>2</sup> The two HXI systems are referred to as HXI1 and HXI2, individually paired with HXT1 and HXT2, respectively. Due to the focusing optics, the sensitivity

\*Address all correspondence to: Kouichi Hagino, E-mail: [hagino@rs.tus.ac.jp](mailto:hagino@rs.tus.ac.jp)

of the hard x-ray imaging system for the point source is 100 times better than those of nonfocusing instruments in the hard x-ray bands, such as hard x-ray detector onboard Suzaku (Suzaku/HXD).<sup>4</sup>

The HXI is composed of a stacked semiconductor imager<sup>5–8</sup> and active shields surrounding the imager. The imager consists of five layers of double-sided strip detectors (DSD) with a strip pitch of 250  $\mu\text{m}$  and detector area of  $32 \times 32 \text{ mm}^2$ . The upper four layers are the double-sided Si strips detectors (DSSDs) with a thickness of 500  $\mu\text{m}$ ,<sup>9–11</sup> and the bottom layer is the CdTe double-sided strip detector (CdTe-DSD) with a thickness of 750  $\mu\text{m}$ .<sup>12–16</sup> The DSSDs have p- and n-type strips on the surface of the top and bottom sides of an n-type Si wafer, while the CdTe-DSDs have Pt- and Al-strips on those of a p-type CdTe wafer. By applying positive bias voltages to the n-side of the DSSDs and the Al-side of the CdTe-DSDs, holes and electrons generated by the incident x-ray photon are collected by the p-side/Pt-side strips and the n-side/Al-side strips, respectively. The x-ray-induced charge on the strip electrodes is read-out utilizing dedicated low-noise front-end application-specific integrated circuits (ASICs),<sup>17</sup> which are connected to the individual strips. The active shields consist of nine  $\text{Bi}_4\text{Ge}_3\text{O}_{12}$  (BGO) scintillators arranged as a well-type structure. Their thicknesses are typically  $\approx 3 \text{ cm}$  in order to stop protons with energy  $\lesssim 100 \text{ MeV}$ , trapped at the South Atlantic Anomaly (SAA). The scintillation light of each BGO is read-out by an avalanche photodiode (APD).<sup>18</sup> By processing the read-out signals from the APDs in digital filters, veto signals are generated and used for reducing the detector background.<sup>19</sup>

Although the HXI was lost,<sup>2</sup> thorough investigations and evaluations of its in-orbit performance are of great importance for planning and designing future hard x-ray missions. In this paper, we describe the in-orbit performance and calibration results of the HXI. In Sec. 2, in-orbit operations and functionalities are summarized. Standard analysis method of the HXI is described in Sec. 3. Detailed performances on the non-x-ray background (NXB) and energy response are presented in Secs. 4 and 5.

## 2 In-Flight Operations

### 2.1 Initial Operations and Observations

After the deployment of the extensible optical bench on February 28, 2016, the temperature of the HXI was gradually cooled to the operation temperature of  $-25^\circ\text{C}$ . On March 8, 2016, a start-up operation of the HXI started. High voltages of the APDs and the DSSD/CdTe-DSD were applied one by one and reached the optimum values on March 12 for HXI1 and March 14 for HXI2.

After being turned on, the HXI performed several observations as listed in Table 1. In spite of the short lifetime of the HXI, x-ray photons from three astronomical objects (IGR J16318–4848, G21.5–0.9, and Crab Nebula) were successfully detected. As well as these data, the HXI observed 164.3 ks (HXI1) and 163.8 ks (HXI2) of blank sky data and 158.7 ks (HXI1) and 160.5 ks (HXI2) of Earth occultation data, including both bright and night Earth. According to the hard x-ray observations by “Swift,”<sup>20</sup> count rate on the HXI due to the albedo x-ray/gamma rays is estimated to be less than  $\sim 10^{-5} \text{ counts s}^{-1} \text{ keV}^{-1} \text{ cm}^{-2}$ . Since this count rate is negligible compared with the background rate as shown in Sec. 5, the Earth occultation data are referred to as the NXB in this paper. On the other hand, the summed data of observation sequences named “None2,” “IRU check out,” and

“RXJ1856.5–3754,” which includes the cosmic x-ray background (CXB), are referred to as blank sky. These background data provide fruitful information on the in-orbit background properties in the hard x-ray energies as described in Sec. 5.

### 2.2 Basic Characteristics

In orbit, all the basic functions of the HXI worked properly. Here, functionalities of the HXI in flight are briefly summarized. For more details, please refer to Nakazawa et al.<sup>2</sup> In the imagers, there was no damage or degradation due to the launch. All read-out channels of all the ASICs worked properly, and noise levels were consistent with the ground calibration. The energy resolution was evaluated by fitting the onboard calibration source spectra, which was mounted just above the top layer of the DSSD. From these data, good energy resolutions of 1.0 keV at 13.9 keV and 2.0 keV at 59.5 keV in full-width at half-maximum were obtained. Also, the energy gain was very stable within an uncertainty of  $< 1$  bin of the pulse-height invariant (PI) at 59.5 keV, corresponding to 0.1 keV or  $\sim 0.2\%$ .

The active shields also showed good performances. The low-energy threshold of each BGO scintillator was the same as the ground calibration results, and anticoincidence rate was consistent with the prelaunch estimation. Light curves of the veto signals from the active shields clearly showed variability corresponding to the geomagnetic cutoff rigidity and decay of the activation component after passages of the SAA. It indicated that the active shields properly monitored the variability of cosmic-ray in the geomagnetic cutoff rigidity and SAA.

## 3 Analysis Method

In this section, the standard analysis method for the HXI data is summarized. It is composed of four steps: gain correction, event reconstruction, screening, and dead-time correction.

### 3.1 Gain Correction

In the gain-correction process, gain-corrected Energy PI (EPI; PI in units of keV, in real number) is calculated. The EPI is generated from the raw analog to digital converter (ADC) value in the gain-correction process and used only in the event reconstruction process. After the event reconstruction, the EPI is converted into PI (in integer number), which is used in further screening and scientific analysis. The relation between PI and EPI is expressed as  $\text{PI}/10 < \text{EPI} < (\text{PI} + 1)/10$ . For example,  $\text{EPI} = 23.17 \text{ keV}$  ( $\text{CdK}\alpha_1$  line) is converted to  $\text{PI} = 231$ .

At the first step of the gain correction, all signals from bad channels are excluded from the following processes. In the flight models, only strips located at the edge of the detector, where the leakage current is higher than the other strips, are defined as bad channels. Thus, the detector area within  $31.5 \times 31.5 \text{ mm}^2$  (126 strips  $\times$  126 strips) is available for imaging spectroscopy, which corresponds to  $9'.03 \times 9'.03$ . Then, the common mode noise is subtracted from ADC values, before correcting the gain. The common mode noise is a noise where all channels in one read-out ASIC coherently fluctuate. It is estimated in the ASICs by recording the median ADC value, which is 16th smallest in all channels in one ASIC. By the common mode subtraction, the pedestal level of each channel is corrected to zero. Finally, the ADC values of good strips are converted to EPI with third-order polynomial functions.

The gain-correction functions are determined based on the ground calibrations conducted in December and October 2014

**Table 1** Observation log of the HXI.

Start time	Stop time	OBSID	Target name	Notes
03-11 21:24	03-13 17:56	10042020–10042030	IGR J16318–4848	HXI1 on
03-13 17:56	03-14 16:20	100042040	IGR J16318–4848	Stray light
03-14 16:20	03-14 18:00	000007010	None2	—
03-14 18:00	03-15 17:56	000007020	None2	HXI2 on
03-15 17:56	03-16 19:40	000008010–000008060	IRU check out	—
03-16 19:40	03-19 17:00	100043010–100043040	RXJ1856.5–3754	—
03-19 17:00	03-23 13:30	100050010–100050050	G21.5–0.9	—
03-23 13:30	03-24 11:22	100043050	RXJ1856.5–3754	—
03-24 11:22	03-25 11:28	100043060	RXJ1856.5–3754	DTHR <sup>a</sup> changed
03-25 11:28	03-25 18:01	000007010–000007020	Crab	—

<sup>a</sup>DTHR is the ASIC ADC digital thresholds for reducing the data size.

for HXI1 and HXI2, respectively. The two HXIs were operated in a low-temperature chamber at Institute of Space and Astronautical Science, where x-ray/gamma-ray photons from radioactive isotopes <sup>241</sup>Am, <sup>133</sup>Ba, <sup>57</sup>Co, and <sup>55</sup>Fe irradiated the instrument. From these data, the correspondence between ADC values and photon energies for x-ray and gamma-ray lines is obtained and listed in Table 2. Between these lines, the ADC-energy correspondence is interpolated with third-order spline functions, which are used as the gain-correction function.

### 3.2 Event Reconstruction

To obtain photon information from the gain-corrected signals in each data acquisition, event reconstruction processes are essential because the HXI imager consists of a stacked double-sided detector. In DSDs, data acquisition for one x-ray photon event usually consists of at least two signals, one each from both sides, and these signals often split into two adjacent strips. Moreover, some signals are detected in multiple layers due to Cd/Te fluorescence lines or Compton scattering. To identify these multi-signal events, all the signals exceeding the digital thresholds (DTHR) are read-out simultaneously from all ASICs in all layers even when only one strip in one layer generates the trigger signal. In the standard HXI analysis, the events are reconstructed as shown in Fig. 1: the gain-corrected EPI in each side is obtained at first, then they are combined within one layer, and then combined with information from other layers to finally reconstruct a photon event.

In the first step, all the signals below analysis thresholds are discarded. The analysis thresholds are larger than DTHR for almost all of the strips and are set to individual strips, to be four times (DSDs) or six times (CdTe-DSDs) the standard deviation of pedestal peaks, which correspond to events with zero energy. Thus, the analysis threshold of the DSDs is much lower than that of the CdTe-DSDs in order to lower the HXI energy range as far as possible. Under these settings, pedestals from all 126 active strips are below the analysis threshold with probabilities of 99.6% for DSDs and more than 99.9999% for CdTe-DSDs. It means that the noise contaminates with probabilities of 0.4%

for DSSD and  $<10^{-4}\%$  for CdTe-DSD. Mean values of the analysis thresholds of all the strips in the bottom sides (*n*-sides) of the top-layer DSSD are 3.56 keV for HXI1 and 3.66 keV for HXI2, and they typically distributes from 3 to 4 keV. These values determine lower limits of the energy range of the HXI because noise levels of the bottom sides are worse than those of the top sides in the DSSDs. Thus, the HXI can observe 5 keV in almost all the strips, while there are two strips with analysis thresholds exceeding 5 keV in HXI2. After applying the analysis thresholds, only signals from the single

**Table 2** X-ray and gamma-ray lines used for gain calibration.

Layer	Side <sup>b</sup>	Lines (keV)
0	Top	5.9, 13.9, 17.8, 20.8, 26.3, 30.8, 35.0, 59.5, 81.0, 122 <sup>a</sup>
	Bottom	5.9, 30.8, 59.5, 81.0 <sup>a</sup> , 122 <sup>a</sup>
1	Top	13.9, 17.8, 20.8, 26.3, 30.8, 35.0, 59.5, 81.0, 122 <sup>a</sup>
	Bottom	30.8, 59.5, 81.0 <sup>a</sup> , 122 <sup>a</sup>
2	Top	13.9, 17.8, 20.8, 26.3, 30.8, 35.0, 59.5, 81.0, 122 <sup>a</sup>
	Bottom	30.8, 59.5, 81.0 <sup>a</sup> , 122 <sup>a</sup>
3	Top	13.9 <sup>a</sup> , 17.8, 20.8, 30.8, 35.0, 59.5, 81.0, 122 <sup>a</sup>
	Bottom	30.8, 59.5, 81.0 <sup>a</sup> , 122 <sup>a</sup>
4	Top	17.8 <sup>a</sup> , 30.8, 35.0, 59.5, 81.0, 122
	Bottom	17.8 <sup>a</sup> , 30.8, 35.0, 59.5, 81.0, 122, 136 <sup>a</sup>

<sup>a</sup>Spectra from sum of all the channels in one ASIC are used for gain calibration, because of lack of the number of photons.

<sup>b</sup>Top and bottom sides of the DSSD are the p- and n-side, and those of the CdTe-DSD are Pt- and Al-side, respectively.

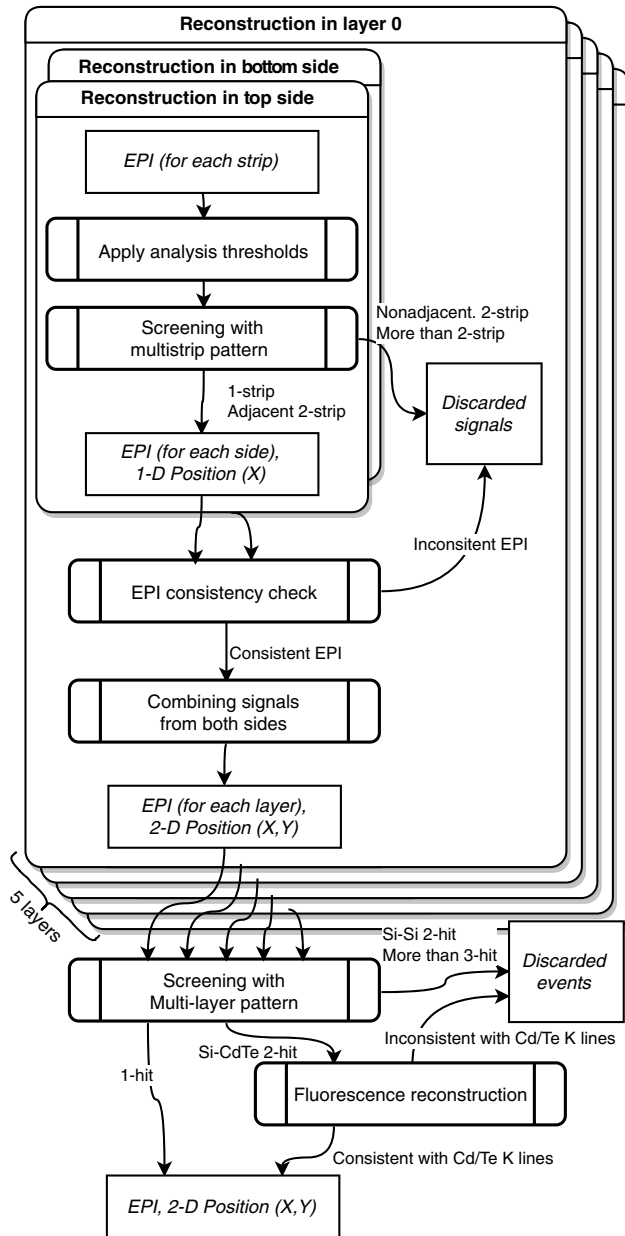


Fig. 1 Overview of the event reconstruction of the HXI.

strip or two adjacent strips are accepted, and signals from more than two strips and those from nonadjacent two strips are discarded. These events are  $<2\%$  to  $3\%$  of all the events in the ground data using radioisotopes.

Since the HXI is composed of double-sided detectors, signals from top and bottom sides of the layer must be combined to obtain two-dimensional (2-D) positional information. EPI from the top side in the DSSDs and that from the bottom side in the CdTe-DSD has better energy resolutions and, thus, is assigned as the EPI value of each layer. Position is simply determined using an intersection point of strips in both sides. When two adjacent strips have signals, the strip with larger pulse height is assigned.

When combining the signals from both sides, consistency between EPI values from both sides is checked using a condition shown in red lines in Fig. 2. Non-x-ray signals by the instrumental noise or a certain cosmic particles can be rejected by this

consistency check. The condition for this check is that the pulse heights (EPI) from both sides match within  $5\sigma$  of the energy resolution. Specifically, it is written as

$$p_0 \text{EPI}_{\text{bot}} - 5\sigma_{\text{bot}} \leq \text{EPI}_{\text{top}} \leq \text{EPI}_{\text{bot}} + 5\sigma_{\text{bot}}, \quad (1)$$

where  $\sigma_{\text{bot}} = \sqrt{p_1^2 + p_2 \text{EPI}_{\text{bot}}}$  is a value to represent the energy resolution of the bottom side. The energy resolution is composed of the energy-independent noise component  $p_1$  and the Fano noise  $\sqrt{p_2 \text{EPI}_{\text{bot}}}$ . Since the noise level of the bottom side is typically 1.0 keV, we set  $p_1 = 1.0$  keV. The parameter  $p_2$  for the Fano noise is a product of the Fano factor  $F$  and the electron-hole pair production energy  $\epsilon$ . By assuming  $F = 0.1$ <sup>21,22</sup> for both Si and CdTe, the second parameters are calculated as  $p_2 = F\epsilon = 0.00036$  keV (Si) and  $0.00044$  keV (CdTe), where the pair production energies of  $\epsilon = 3.6$  eV (Si) and  $4.4$  eV (CdTe)<sup>12</sup> are used. In addition to these parameters, the low mobility of holes in CdTe is taken into account as a parameter  $p_0$  by assuming that every 7.1% of charges are lost during the drift toward the Pt-side strips from the incident position. Thus,  $p_0 = 0.929$  for CdTe-DSD and  $p_0 = 1.0$  (complete charge collection) for DSSD are assumed. In DSSDs, subpeak events due to the nonuniform electric field,<sup>9</sup> which is described in Sec. 4, are also discarded by this process. In the on-ground calibration experiment using <sup>241</sup>Am radioisotope, 2% to 3% of total events in DSSDs and  $\sim 1\%$  in CdTe-DSDs are discarded.

After finishing the event reconstruction processes in one layer, hits in five layers are reconstructed as a photon event. In this process, single-hit events detected in a single layer and double-hit events at the combination of one CdTe-DSD and one DSSD with an energy of DSSD consistent with a fluorescence line of Cd or Te are accepted. Otherwise, no values are assigned to PI, hit positions in the final event list and hence discarded in the following processes. In terms of physical processes, this algorithm accepts photoabsorption events and fluorescence escape events, where K-shell fluorescence photons of Cd or Te escaped from CdTe-DSDs are photoabsorbed in DSSDs. Compton scattered events are ignored in current implementation because a fraction of such events composed of Si-Si double hits or Si-CdTe nonfluorescence double hits in total events are less than  $\sim 1\%$  in the ground data obtained with <sup>241</sup>Am and <sup>133</sup>Ba radioisotopes.

The event reconstruction algorithm described above must be tested with in-flight data because it was determined based on the ground data analysis. For the purpose of investigating whether this algorithm properly rejects the background data without excluding much of the real x-ray signals, fractions of accepted events (black) and discarded events (red and blue) of the ground calibration data (trigger rate  $\approx 630$  Hz), Crab data (trigger rate  $\approx 610$  Hz), and the NXB data (trigger rate  $\approx 35$  Hz) are shown in Fig. 3. In this figure, the denominator of the fractions is the number of events, in which at least one signal exceeds the analysis thresholds. The nonsignal events account for  $5.341\% \pm 0.007\%$  of ground calibration data,  $25.27\% \pm 0.02\%$  of Crab data, and  $97.680\% \pm 0.008\%$  of the NXB data. These nonsignal events are thought to originate from noise triggers and soft photons below the analysis thresholds because trigger thresholds are set to be as low as possible within a range where the dead-time fraction due to noise triggers does not affect the scientific observations. The reason it is very high in the NXB data is simply because its trigger rate by the external photon and particle

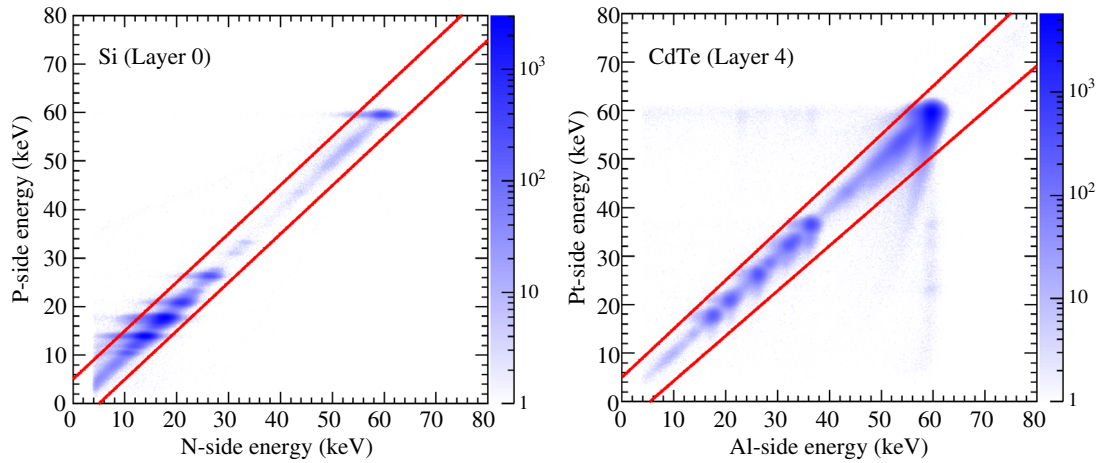


**Fig. 2** Criteria for the consistency check between EPI values from both sides (red lines). Color maps show 2-D histograms of the EPIs of HXI2 obtained from the ground calibrations irradiated by x-rays from  $^{241}\text{Am}$ .

background is much lower than those by the instrumental noise (typically a few Hz).

From Fig. 3, the fraction of discarded events over all nonzero signal events is much larger in the NXB data than the ground calibration and Crab data. All inconsistent EPI, nonadjacent 2-strip and  $\geq 3$ -strip are contained in the NXB data, indicating non-x-ray origins of the signal. On the other hand, more than  $\approx 95\%$  of events are accepted in ground calibration and Crab data, which are presumably dominated by x-ray signals. Thus, in other words, the multilayer nature of the imager and the event reconstruction procedure using their information are effective in reducing the background.

### 3.3 Screening

In addition to the event reconstruction process, bad events (e.g., veto events) and bad time intervals (e.g., SAA passages), which are presumably dominated by the instrumental noise or the NXB, are excluded both in the onboard software and the ground analysis software. Basically, the in-flight screening is less

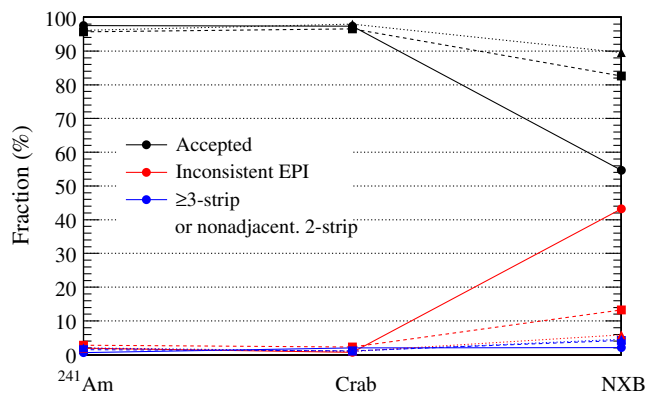


**Fig. 3** Fractions of each event type in the reconstruction for top-layer DSSD (layer 0), the other DSSDs (layers 1 to 3), and CdTe-DSSD (layer 4) among the nonzero signal events. HXI2 data of ground calibration, Crab observation, and NXB are used. Filled circles with solid lines, squares with dashed lines, and triangles with dotted lines denote the layer 0, layer 1 to 3, and layer 4, respectively.

stringent than the on-ground screening to flexibly change the screening conditions after observations, on the ground.

The in-flight screening of the HXI is performed in ASICs and HXI Digital Electronics (HXI-DE). In ASICs, only signals exceeding a predefined DTHR are read-out. DTHR is adjustable for each ASIC independently and is also independent from the trigger threshold. On the day before the Crab observation, it was raised up to similar level to the ground-software analysis thresholds for reducing the data size. Read-out data from the ASICs are reduced by further screening in HXI-DE. It assigns “CATEGORY” of high, middle, and low to each event. Assignment of the CATEGORY is performed using the time interval from the previous trigger, number of signals above DTHR, ADC values, flags of active shield coincidence, trigger pattern, and the other flags from the ASIC. This CATEGORY determines priorities to record the event to the data recorder (DR) of the satellite. Since the capacity of the DR is limited, most of the data in middle and low categories are not downloaded to the ground except for those obtained within the interval the satellite is in direct contact with from the operation site at Uchinoura in Japan.

In all observations of the HXI, the screening criteria as listed in Table 3 are applied in HXI-DE. If an event has a flag for the calibration source signal, pseudotrigger, test pulse, or forced trigger, CATEGORY = High is assigned automatically. Then, CATEGORY = Low is assigned to an event if it has a flag of fast BGO, number of signals exceeds 31, which cannot happen with x-ray photons, or any of signals has ADC value of 1023, which is the upper limit of ADC. In the remaining events, if a signal has a flag of HITPAT (hitpattern) BGO, CATEGORY = Middle is assigned. While the fast BGO signal is a veto signal capable to stop ADC conversion if needed, the HITPAT BGO signal is slow but a lower threshold veto signal is to be used for further background rejection in the on-ground data screening (see Ohno et al.<sup>19</sup> for more details). Finally, CATEGORY = High is assigned to all the remaining events. In this screening, only events that are almost certainly the background signals are classified to middle or low categories.

The in-flight screening criteria by HXI-DE should also be tested with the Crab and NXB data. In the Crab observation, fractions of high, middle, and low categories are 93.8%, 1.7%, and 4.5%, respectively. Here, these fractions are calculated from

**Table 3** Criteria for each CATEGORY.

CATEGORY	Criteria
High	Calibration source, pseudotrigger, test pulse or forced trigger
	Not assigned to middle or low
Middle	Flagged as HITPAT BGO and not flagged as fast BGO
Low	Flagged as fast BGO
	Number of signals >31
	Any of signal has ADC = 1023

the number of events categorized as high/middle/low, which are recorded in the housekeeping data even when the event data are not downloaded. On the other hand, in NXB observations, those are 53.7%, 1.5%, and 44.8%, respectively. The fraction of middle category is very small as expected. Since the low category contains only background-like events, it is expected that more events are classified to low category in the NXB observation than the Crab observation. More detailed screening is applied to the HXI data in the on-ground pipeline analysis. In the standard screening criteria for the scientific observations, time intervals at or around the SAA passages and those in Earth occultations are excluded. After the launch of the satellite, a new screening condition  $SAA2\_HXI=0$  is added to the standard screening to reduce the background in top-layer DSSDs, which is described in Sec. 5.

Since the HXI imager is a multilayer detector, an energy-dependent layer selection is applied for maximizing its sensitivity (signal-to-noise ratio). As shown in Fig. 4, the detection efficiency strongly depends on the layer as well as the incident x-ray energies. For example, the top-layer DSSD (layer 0) is capable of detecting only low-energy photons, typically below 30 keV, whereas the CdTe-DSD (layer 4) covers energies above ~20 to 30 keV. Although the best detection efficiency can be achieved using all the layers in all energy bands, the background level would inevitably be maximized. Thus, to maximize the sensitivity of the HXI, the energy-dependent layer selection is necessary. As explained in detail in Sec. 5, the NXB of the top-layer DSSD (layer 0) is different from DSSDs in the other layers due to the electron background, while those in the middle layers (layer 1 to 3) are very similar to each other. Thus, the HXI imager is separated into three groups, layer 0, layer 1 to 3, and layer 4, and their sensitivities are estimated using the in-orbit NXB spectra and the effective area. To optimize these sensitivities, only events satisfying conditions of  $PI < 300$  for top-layer DSSD (layer 0),  $120 \leq PI$  for the DSSDs in lower layers (layer 1 to 3), and  $300 \leq PI$  for the CdTe-DSD (layer 4) are accepted. These correspond to <30 keV for the top-layer DSSD, 12 to 80 keV for the DSSDs in lower layers, and >30 keV for the CdTe-DSD.

### 3.4 Dead-Time Correction

The dead-time correction of the spectra and light curves of the HXI is performed by utilizing pseudoevents.<sup>23</sup> The pseudoevents are the events triggered by the pseudotrigger, which is

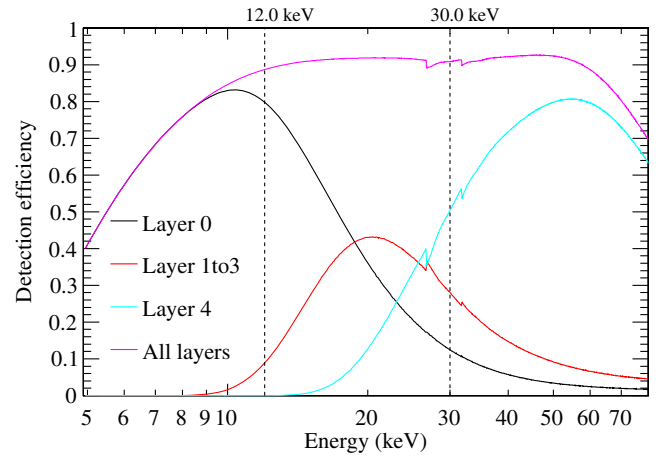


**Fig. 4** Detection efficiency of top-layer DSSD (layer 0), the other DSSDs (layers 1 to 3), and CdTe-DSD (layer 4). By the energy-dependent layer selection, only events with  $PI < 300$  for layer 0,  $120 \leq PI$  for layers 1 to 3, and  $300 \leq PI$  for layer 4 are accepted. The PIs of 120 and 300 correspond to energies of 12 and 30 keV shown by dotted lines.

generated with a random time interval in the onboard FPGA in HXI Analog Electronics. Frequency of the pseudotrigger is set to be 2 Hz by default. Since the pseudoevents are treated in the same manner as normal events triggered by the ASICs, the number of pseudoevents passing through the data screening divided by the number of input pseudotriggers is a good estimate for the live-time fraction. The process of the dead-time correction is implemented in a dedicated tool `hxisgddtime`.

The average dead-time per event in the HXI is  $\approx 370 \mu\text{s}$  based on the Crab observation data. It is dominated by reset wait time ( $250 \mu\text{s}$ ), which is a wait time to return to the state for waiting for the next trigger after the previous data acquisition in order to avoid triggering the noise induced by the AD conversion of the previous event. The other components of the dead time are the AD conversion ( $\approx 20$  to  $200 \mu\text{s}$ , depending on the pulse height), data transfer from ASICs to the FPGA ( $\approx 20$  to  $40 \mu\text{s}$ , depending on the number of signals above the DTHR for one trigger) and so on. In addition to the dead time accompanying each event, events in accidental coincidence with BGO active shields generate the dead time.

In the Crab observation, dead-time fractions estimated by the pseudoevents are 23.4% and 26.2% for HXI1 and HXI2, respectively. Their uncertainties are 1% to 2% point due to the inherent statistical uncertainties of the number of random pseudoevents. Then, we verified this number with independent estimation. Since the trigger rates of HXI1 and HXI2 are  $572.44 \pm 0.26$  Hz and  $613.06 \pm 0.27$  Hz, respectively, fractions of the dead time depending on the event rate are calculated as  $f_{dt} = \tau f = 21.0\%$  and  $22.9\%$ . Here,  $\tau$  is the mean dead-time per event ( $367 \mu\text{s}$  for HXI1 and  $374 \mu\text{s}$  for HXI2) and  $f$  is the trigger rate. In addition to this, the fraction of the accidental coincidence with the BGO is estimated using the number of events classified to low or middle. By assuming that rates of low or middle events in the Earth occultations do not include the accidental coincidence events, but they are included in the low/middle events in the Crab observation, rates of the accidental coincidence events in the Crab observation are estimated by subtracting the low/middle rates in the Earth occultations (15.2 Hz for HXI1 and 15.5 Hz for HXI2) from those in the Crab observations (38.5 Hz for HXI1 and 38.1 Hz for HXI2). The accidental

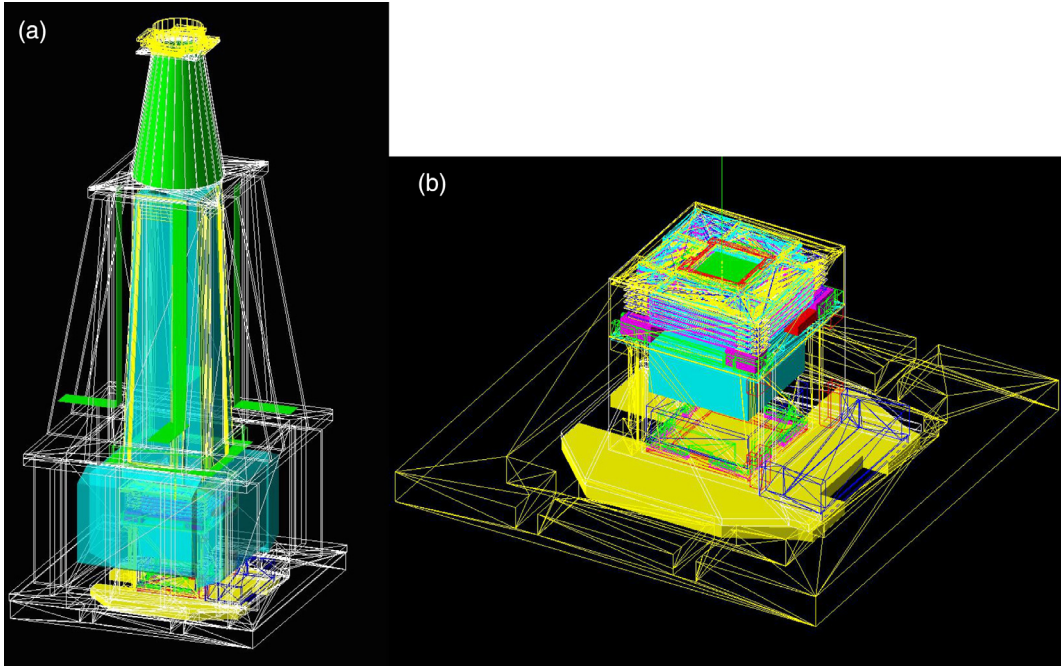


**Fig. 5** (a) Geant4 mass model of the HXI and that of the (b) imager module for the detector response simulations.

coincidence rates are calculated to be 23.3 Hz for HXI1 and 22.6 Hz for HXI2, meaning that 4.05% and 3.69% of the trigger rate are discarded, respectively. Thus, by considering the accidental coincidence events, the dead-time fraction is estimated to be 24.2% for HXI1 and 25.7% for HXI2, which match to those estimated by the pseudoevents within the statistical uncertainties.

## 4 Energy Response Matrix

### 4.1 Simulations of Detector Devices

The response matrix of the HXI is constructed by running Monte Carlo simulations since Compton scattering and secondary emissions are nonnegligible in hard x-ray bands. The simulation is composed of two steps: (1) Monte Carlo simulations for calculating the interactions of x-ray photons with detectors and passive materials in the HXI system and (2) calculations of charge transportation in the semiconductor detectors. This simulation code is based on an integrated response generator “ComptonSoft,”<sup>24</sup> which is available in GitHub repository: <https://github.com/odakahirokazu/ComptonSoft>.

The Monte Carlo simulation part is based on the Geant4 toolkit library,<sup>25,26</sup> which is widely used for the particle tracking in high-energy physics. Figure 5 shows a detailed Geant4 mass model of the HXI implemented in the detector response simulations. Since all the materials in the HXI system affect the detector response, most of the passive materials as well as the imager module and BGO active shields are included in the mass model. The Monte Carlo simulations are performed for each energy bin of the response matrix with monochromatic photons at the central energy of the bin. The incident photons for the simulations are generated in a horizontal plane with the detector size ( $32 \times 32 \text{ mm}^2$ ) located above the HXI-S entrance window, with an initial direction to the detector along the optical axis.

After the Monte Carlo simulations, the energy deposits obtained in the simulations are spread by considering the thermal diffusion. In this simulation, it is spread by the 2-D Gaussian with  $\sigma = f_{\text{diff}} \sqrt{2k_B T \mu t / e}$ , where  $k_B$  is the Boltzmann constant,  $T$  is the temperature of the detector, and  $t$  is the drift time from carrier creation to arrival to the electrodes. An additional factor  $f_{\text{diff}}$  is introduced to reproduce experimental results. Since it only considers the thermal diffusion, this factor represents an effect by the Coulomb repulsion.<sup>27,28</sup>

Using the spread energy deposits, the induced charge on each read-out strip is calculated with the simulation of the charge transportation. The induced charge  $Q$  is calculated utilizing a weighting potential  $\phi_w$  derived from the Shockley–Ramo theorem<sup>29</sup> as

$$Q = - \int q(x) \nabla \phi_w(x) \cdot dx, \quad (2)$$

where  $q(x)$  is a charge inside the detector and  $\int dx$  is an integration along the trajectory of the charge  $q(x)$  to the read-out electrode. By considering the finite lifetime  $\tau$  and mobility  $\mu$  of carriers and assuming a uniform electric field  $E$  in the detectors, the induced charge is written as

$$Q = -q_0 \int_{z_i}^{z_f} \exp\left(-\frac{z - z_i}{\mu \tau E}\right) \frac{\partial \phi_w(x, z)}{\partial z} dz, \quad (3)$$

where  $z_i$  and  $z_f$  are the initial and final positions of the charge, respectively, and  $q_0$  is the initial charge. The strip electrodes are lined up in  $x$ -direction and  $z$ -axis points down into the detector. The induced charge is calculated by multiplying the energy deposits and the charge collection efficiency defined as a sum of  $Q/q_0$  for holes and electrons, which depends on the interaction position.

The weighting potential is a solution of Laplace’s equation with the boundary condition of  $\phi_w = 1$  at the read-out electrode

and  $\phi_w = 0$  at all the other electrodes. That for the strip detectors is calculated as

$$\phi_w(x, z) = \sum_{m=1}^{\infty} A_m \sin(\alpha_m x) \sinh(\alpha_m z), \quad (4)$$

$$A_m = \frac{2}{m\pi \sinh(\alpha_m L)} f_m, \quad (5)$$

$$f_m = \cos\left[\frac{\alpha_m(a-U)}{2}\right] - \cos\left[\frac{\alpha_m(a+U)}{2}\right], \quad (6)$$

where  $\alpha_m = m\pi/a$ ,  $a$  is the detector size,  $U$  is the strip pitch, and  $L$  is the thickness of the detector. In the case of the HXI CdTe-DSDs,  $a = 32$  mm,  $U = 250$   $\mu\text{m}$ , and  $L = 750$   $\mu\text{m}$ . By combining Eq. (3) with Eq. (4), the charge collection efficiency of CdTe-DSD is calculated.

The response of the HXI DSSDs is more affected by charge loss due to the complicated electric field structure inside the detector rather than the charge trapping due to finite lifetime of the carriers described in Eq. (3). Since a mobility-lifetime product ( $\mu\tau$ ) of carriers in Si is 2 to 3 orders of magnitude larger than that of CdTe, it is assumed to be infinite in this simulation, which is equivalent to the charge correction efficiency of unity. On the other hand, a significant fraction of the charge is lost by local minimum of the electric potential due to a positive fixed charge on the Si-SiO<sub>2</sub> surface at gaps among strip electrodes.<sup>9,30</sup> It makes a subpeak at  $\simeq 1/2$  of the incident x-ray energy in the top side of DSSD, negative peak in the adjacent strip, and no signals in the bottom side of DSSD. Thus, we refer to these events as subpeak events. The subpeak events are unusable for the event reconstruction because they do not have any information of the position in the bottom side. Specifically, they are

discarded in the consistency check between EPI values from both sides [Eq. (1) and Fig. 2]. Since the potential local minimum is located on the surface of the top side of the detectors, this effect reduces the detection efficiency at energies below  $\sim 10$  keV. This effect is simply implemented as rectangular dead regions located at the strip gaps on the surface of the DSSD in our simulation. All induced charges corresponding to energy deposits in these dead regions are set to be zero.

## 4.2 Simulation Parameters

All the parameters of the detector simulations for constructing the response matrix are listed in Table 4. The bias voltage, the mobility-lifetime products  $\mu\tau$  of holes and electrons, the diffusion factor, and the noise level of each strip are required for both CdTe-DSD and DSSDs, and one additional parameter for subpeak events is required for DSSDs. In addition to these, trigger efficiency, which reduces the detection efficiency at the lower energy end due to the energy resolution in the shaper for the trigger generation, and absorption by SiO<sub>2</sub> layers on surface of the DSSDs are multiplied to the energy response. The parameters used in the HXI response simulations are determined based on the ground calibration data of flight model and engineering model of the HXI. The mobility-lifetime product  $\mu\tau$  of CdTe-DSD is determined by fitting spectra of the single layer experiment of the engineering model detectors. The diffusion factor  $f_{\text{diff}}$  is set to be 2 as it reproduces the engineering model data. The noise parameter of each channel is estimated from the linewidths of an x-ray line at 59.5 keV from <sup>241</sup>Am obtained in the ground calibration tests of the flight model detectors. Although only mean values of the noise levels from all the strips are listed in Table 4, the noise level is assigned strip by strip in the simulation.

**Table 4** Simulation parameters for the HXI detector response.

Parameters <sup>a</sup>	Values					
	HXI1			HXI2		
Layer	0	1 to 3	4	0	1 to 3	4
Bias (V)	250	250	250	250	250	350
$(\mu\tau)_h$ (cm <sup>2</sup> V <sup>-1</sup> )	$\infty$	$\infty$	$1.54 \times 10^{-4}$	$\infty$	$\infty$	$1.54 \times 10^{-4}$
$(\mu\tau)_e$ (cm <sup>2</sup> V <sup>-1</sup> )	$\infty$	$\infty$	$1.41 \times 10^{-3}$	$\infty$	$\infty$	$1.41 \times 10^{-3}$
$d_{\text{subpeak}}$ ( $\mu\text{m}$ )	25	25	—	25	25	—
$f_{\text{diff}}$	2	2	2	2	2	2
$d_{\text{SiO}_2}$ ( $\mu\text{m}$ )	5	4	—	3	4	—
$E_{\text{trig}}$ (keV)	2.97	—	—	3.05	—	—
$\sigma_{\text{trig}}$ (keV)	0.92	—	—	0.70	—	—
Top-side noise (keV)	0.86	0.90	1.71	0.89	0.90	1.84
Bottom-side noise (keV)	2.49	3.04	1.75	2.57	2.92	1.80

<sup>a</sup> $(\mu\tau)_h$  and  $(\mu\tau)_e$  are the mobility-lifetime products of holes and electrons, respectively,  $d_{\text{subpeak}}$  is a thickness of the dead region where the subpeak events are generated,  $f_{\text{diff}}$  is the diffusion factor for spreading carrier clouds,  $d_{\text{SiO}_2}$  is the thickness of the SiO<sub>2</sub> layer on surface of the DSSDs, and  $E_{\text{trig}}$  and  $\sigma_{\text{trig}}$  are the mean energy and  $\sigma$  of an error function for describing the trigger efficiency, respectively.

Detection efficiency at low energies of DSSDs is affected by three effects: subpeak events, trigger efficiency, and absorption by the inactive layer. Size of the dead region due to the subpeak events is assumed to be a rectangle with a width of  $120\ \mu\text{m}$ , which is the same as the width of the gap among the strip electrodes of the DSSDs. By performing experiments using a single layer of the DSSD engineering model, thickness of the dead region  $d_{\text{subpeak}}$  is estimated to be  $25\ \mu\text{m}$  from the energy dependence of the subpeak fraction.<sup>30</sup> Trigger efficiency of the top-layer DSSD is assumed to follow the error function, and its mean energy and  $\sigma$  are estimated by measuring the detected count rate for 5.9-keV line from  $^{55}\text{Fe}$  and its subpeak at 3.2 keV as a function of the trigger threshold in the ASIC. The trigger generation and sample/hold (and then the ADC) are performed in different analog-shaping chains in the ASIC with different shaping times of  $0.6\ \mu\text{s}$  for the former part and  $\approx 3\ \mu\text{s}$  for the latter. The noise level of the trigger  $\sigma_{\text{trig}}$  is usually worse than that of the EPI values corresponding to the spectral resolution. In the other layers, trigger efficiency is not considered because the trigger threshold  $E_{\text{trig}}$  is much lower than the analysis threshold applied in the pipeline process. The thickness of the inactive layer, including  $\text{SiO}_2$  layers and Al electrodes, on the surface of the DSSDs is estimated to be  $\approx 4\ \mu\text{m}$ . Since the difference between photoabsorption cross sections with  $\text{SiO}_2$  and Al is negligible, the inactive layer is treated as a  $\text{SiO}_2$  layer with a thickness of  $d_{\text{SiO}_2}$ . Thus, this value is set to the detectors in layers 1 to 3 as listed in the table.

In addition to the relatively rough estimates of the subpeak fraction, trigger efficiency, and the  $\text{SiO}_2$  thickness, more detailed tuning of these parameters is needed to reproduce the in-flight data, especially around the lower energy end, in which the photon statistics is the highest in many cases. Among these three parameters,  $\text{SiO}_2$  thickness is chosen as a free parameter for adjusting. First, 5 to 12 keV spectra of G21.5–0.9 observed by the SXI and HXI are simultaneously fitted, and the  $\text{SiO}_2$  thicknesses of HXI1 and HXI2 are constrained to be 3.7 to 5.6  $\mu\text{m}$  and 2.5 to 4.4  $\mu\text{m}$  as 90% confidence intervals, respectively. Then, in order to constrain the  $\text{SiO}_2$  thickness more tightly, the 5- to 40-keV Crab spectra of the HXI are fitted using response matrices with  $\text{SiO}_2$  thickness of 4.0, 4.5, 5.0, and 5.5  $\mu\text{m}$  for HXI1 and 2.5, 3.0, 3.5, and 4.0  $\mu\text{m}$  for HXI2. As the result,  $d_{\text{SiO}_2} = 5.0\ \mu\text{m}$  for HXI1 and  $d_{\text{SiO}_2} = 3.0\ \mu\text{m}$  for HXI2 are found to give the best  $\chi^2$  value. Thus, these values are used for constructing the HXI response matrix.

This difference between HXI1 and HXI2 changes the detection efficiency at 5 keV by 7%. Note that this result does not mean that the actual  $\text{SiO}_2$  thickness is different between HXI1 and HXI2. The difference would include all of the effect in the lower energies by the subpeak fraction, trigger efficiency, and the  $\text{SiO}_2$  thickness.

### 4.3 Validation with Ground Calibration Data

For the purpose of testing the response simulation and its parameters, the simulated spectra and their properties are compared with those of the ground calibration data irradiated by x-rays from  $^{133}\text{Ba}$  and  $^{241}\text{Am}$ . The simulations are performed in a geometry with a thermostat chamber and passive materials near the radioisotopes. All the x-ray and gamma-ray lines above 10 keV with emission probabilities larger than 0.1% are simulated. The Lund/LBNL Nuclear Data Search<sup>31</sup> is referred to for the energies and emission probabilities of all the lines from  $^{133}\text{Ba}$  and 26.3 and 59.5 keV from  $^{241}\text{Am}$ , while Lépy et al.<sup>32</sup> is referred to for the other lines from  $^{241}\text{Am}$ .

The simulated spectra and the experimental spectra from the ground calibrations of the HXI flight model are shown in Fig. 6. Spectral shapes, including scattered components, tail structures due to the small  $\mu\tau$  in CdTe, and energy resolutions are well reproduced. Moreover, detection efficiency is consistent within  $\approx 10\%$ , and at higher energies above  $\approx 60$  keV, it matches better than 5%. Here, we should note that the self-absorption effect in the  $^{241}\text{Am}$  source is considered in this simulation by assuming a 5- $\mu\text{m}$ -thick Am as an absorber. Figure 7 shows fractions of the 2-strip events of the simulations and the experiments. These fractions have to match with each other for reproducing the spectral shape because energy resolutions of the 2-strip spectra are worse than those of the single-strip spectra. In other words, if the simulation overestimates the 2-strip fraction, the energy resolution of simulated spectra would be worse than those of the experiments. As shown in the upper panels, the 2-strip fractions are reproduced within 2% of the total event number in DSSD p-side and CdTe-DSD Al-side, whose EPI values are used for the spectral analysis. The discrepancy in CdTe-DSD Pt-side has almost no effects on the scientific analysis because the EPI values from CdTe-DSD Pt-side and DSSD n-side are only used for the consistency check between signals in top and bottom sides in the event reconstruction process.

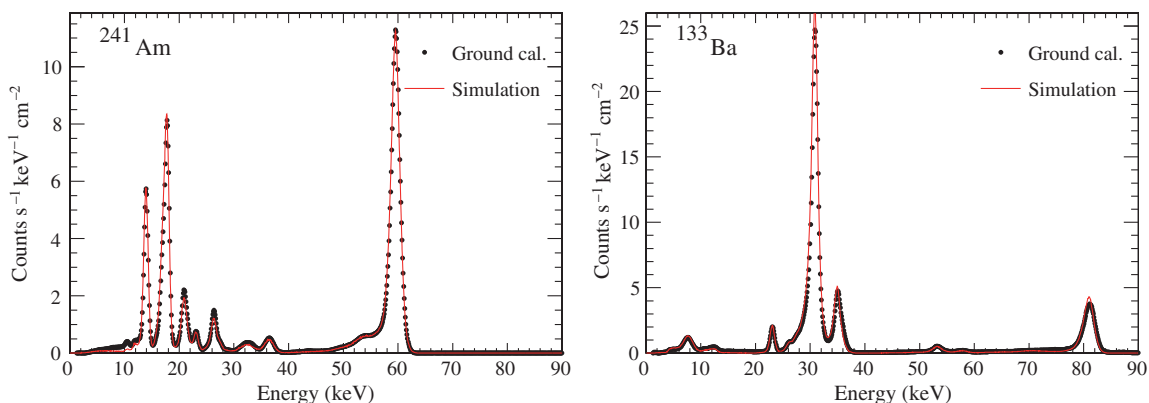


**Fig. 6** HXI2 spectra of x-ray lines from  $^{241}\text{Am}$  and  $^{133}\text{Ba}$ . Black points are the experimental spectra obtained in the ground calibrations of the HXI flight model, and red lines are the simulated spectra.

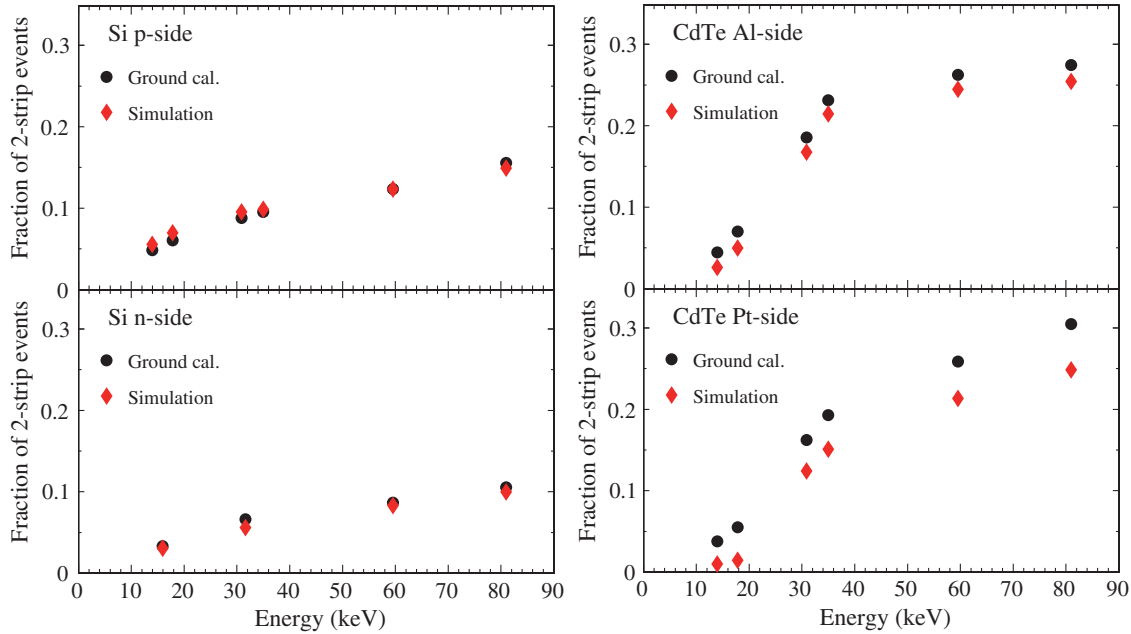


**Fig. 7** Fractions of the 2-strip events as a function of energy in the ground calibration data (black circle) and the simulated data (red diamond).

#### 4.4 Crab Spectra

Using the HXI response matrix described above, the Crab spectra are analyzed. All the standard processing and screenings (see Sec. 3) are applied to the data, and the spectra are extracted from circular regions with a radius of  $4'$ . The background spectra are extracted from the blank sky observations (i.e., None2, IRU check out, and RXJ1856.5–3754), which contain the CXB as well as the NXB. The size of the extraction regions for the background spectra is the same as those for the Crab spectra. Net exposures of the Crab spectra after the dead-time correction are 5.92 ks for HXI1 and 6.14 ks for HXI2, respectively, and  $2.69 \times 10^6$  photons are detected by each of HXI1 and HXI2 in an energy range of 5 to 80 keV.

The Crab spectra observed by the HXI are shown in Fig. 8. They are fitted with an absorbed powerlaw model  $\text{CONSTANT}^* \text{TBABS}^* \text{POWERLAW}$  convolved with the detector response and the telescope effective area using the spectral analysis software XSPEC.<sup>33</sup> As shown in the lower panel in Fig. 8, the deviations between the Crab spectra and the best-fit model are  $<5\%$  at energies below  $\approx 50$  keV. The telescope effective area is measured with uncertainties less than  $\approx 2\%$  on ground<sup>34</sup> and confirmed by the Crab observation.<sup>3</sup> Although both the telescopes and detectors are well calibrated, residuals of  $\sim 13\%$  level are seen above 50 keV. This might be due to calibration uncertainties in the telescope effective area or inappropriate modeling of the detector response.

The best-fit parameters and 90% confidence errors for the HXI Crab spectra are listed in Table 5. A difference of normalizations between HXI1 and HXI2, which is expressed by a constant parameter 0.968, is consistent with unity considering the uncertainty in the dead-time correction. For example, we also applied the independent dead-time correction, as discussed in Sec. 3, which are estimated to be 24.2% for HXI1 and 25.7% for HXI2. If we adopt these values, the powerlaw normalization at 1 keV is  $N = 10.43 \pm 0.04$  photons  $\text{cm}^{-2} \text{s}^{-1} \text{keV}^{-1}$  and a constant parameter is  $f_{\text{HXI2}/\text{HXI1}} = 0.985 \pm 0.001$ .

Our best-fit values of the powerlaw index  $\Gamma = 2.107 \pm 0.002$  and a normalization at 1 keV  $N = 10.54 \pm 0.04$  are consistent with the historical values of  $\Gamma = 2.10 \pm 0.03$  and  $N = 9.7 \pm 1.0$  proposed by Toor and Seward.<sup>35</sup> Also, the spectral slope is consistent with the values of  $\Gamma = 2.10 \pm 0.01$  obtained by Suzaku/HXD PIN with HXD nominal position<sup>23</sup> and  $\Gamma = 2.106 \pm 0.006$  obtained by the large off-axis observations of the Crab by NuSTAR.<sup>36</sup> On the other hand, the normalization is not consistent with either of these observations. Our best-fit normalization is just between  $N = 11.2 \pm 0.09$  by the HXD and  $N = 9.71 \pm 0.16$  by NuSTAR. This result does not immediately mean that the HXI effective area is inconsistent with the other observatories because the Crab flux can vary on a yearly timescale.<sup>37</sup>

#### 4.5 Spatial Dependence of the Detector Response

In addition to the spatially integrated detector response used in the Crab spectral analysis, we also verified the reproducibility of

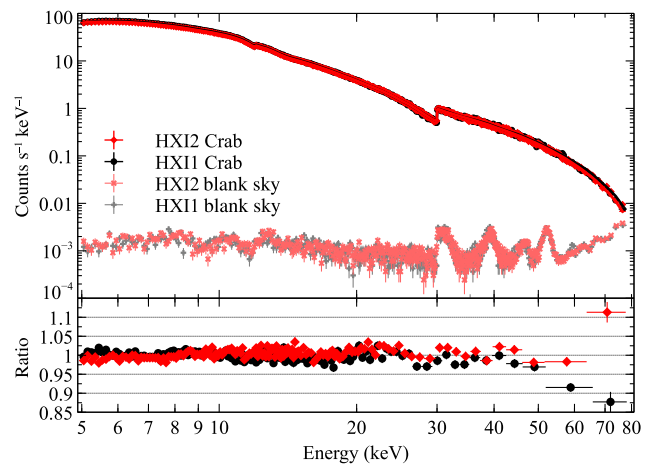


**Fig. 8** Crab and background spectra observed by HXI1 and HXI2 and the ratio between the Crab spectra and an absorbed powerlaw model.

**Table 5** Best-fit parameters and 90% confidence errors of the Crab spectra.

	$N_{\text{H}}$ ( $\text{cm}^{-2}$ )	$\Gamma$	Normalization at 1 keV ( $\text{photons cm}^{-2} \text{s}^{-1} \text{keV}^{-1}$ )	Constant	$F_{3-50 \text{ keV}}$ ( $10^{-8} \text{ erg cm}^{-2} \text{s}^{-1}$ )
HXI1	$3.0 \times 10^{21\text{a}}$	$2.107 \pm 0.002$	$10.54 \pm 0.04^{\text{b}}$	$1.0^{\text{a}}$	$3.647 \pm 0.004$
HXI2				$0.968 \pm 0.001$	

<sup>a</sup>Column density  $N_{\text{H}}$  and the constant factor for HXI1 are fixed.

<sup>b</sup>The statistical uncertainty of the dead time ( $\approx 1\%$  to  $2\%$  in  $1 - \sigma$  confidence level) is not added. It corresponds to the normalization uncertainty of  $\approx 0.2$  to  $0.3$  (90% confidence).

positional difference of the detector response. In the standard analysis tool, the response is separated into the detection efficiency and response matrix. The matrix defines the relation between the incident photon energy and the output EPI values, which correspond to the spectral shape. The spatial dependence of the detection efficiency is implemented for pixel by pixel based on the Monte Carlo simulations of the detector response. On the other hand, the response matrix is integrated over all the detector area in order to reduce data size of response database files. Therefore, the spatial dependence of the detector response is taken into account only by the detection efficiency.

To demonstrate the accuracy of the spatial dependence of the detector response, noisy strips located close to the center of the field of view (FoV) of HXI2 provide a good example. The analysis thresholds of these noisy strips are 5.58 and 6.71 keV, which are much higher than those in the typical strips, 3.66 keV. Due to the higher analysis thresholds, detection efficiencies at low energy in these strips are significantly smaller than the other strips, resulting in a dark line at the center of the image as shown in Fig. 9.

The spectra extracted from a  $20'' \times 540''$  rectangular region covering the noisy strips in HXI2 are shown in the upper panel of Fig. 10. There is a clear difference of the low-energy spectra between HXI1 and HXI2. The count rate at 5 keV in HXI2 is smaller than that of HXI1 by a factor of 1.5 because of the higher analysis thresholds in the noisy strips in HXI2. As shown in the lower panel in Fig. 10, this large difference between HXI1 and HXI2 is reduced to better than  $\pm 5\%$  level by applying

the detector response, which is generated in a standard manner by assuming a point source located at the red cross in Fig. 9. In this analysis, a broken powerlaw model is assumed by following the NuSTAR observations of the Crab pulsar<sup>38</sup> because the selected spectra are strongly affected by it. The best-fit parameters of powerlaw slopes  $\Gamma_1 = 2.029 \pm 0.010$  and  $\Gamma_2 = 2.185 \pm 0.008$ , break energy  $E_b = 10.4 \pm 0.4$  keV, normalization  $N = 7.0 \pm 0.2$   $\text{photons cm}^{-2} \text{s}^{-1} \text{keV}^{-1}$ , and the constant parameter  $f_{\text{HXI2}/\text{HXI1}} = 1.067 \pm 0.004$  are obtained. This result demonstrates the accuracy of the spatial dependence of the HXI detector response.

## 5 Non-X-Ray Background

### 5.1 Properties of DSSD Background

Before the screening of  $\text{SAA2\_HXI}=0$  described in Sec. 3, NXB in top-layer DSSD (layer 0) of the HXI is dominated by a hard powerlaw component as shown in Fig. 11. In pre-launch estimations, NXB in top-layer DSSD is expected to show a similar level with those in the other layers of DSSDs because their background is thought to be mainly caused by albedo neutrons, interacting via elastic scattering.<sup>39</sup> In this sense, the fact that the middle layers (layers 1 to 3) of DSSDs show a similar level is as expected.

The powerlaw component in top-layer DSSD is due to the low-energy albedo electrons for the following two reasons. First, this component extends up to 100 keV as shown in Fig. 11, but lower layers do not show this component strongly.

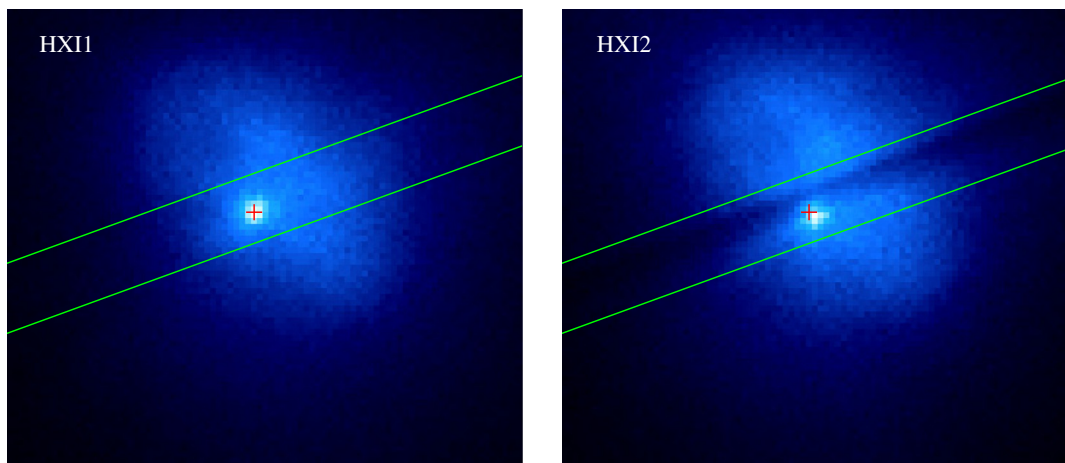


**Fig. 9** Crab images obtained by HXI1 and HXI2. Noisy strips are clearly seen in the HXI2 image. The red cross and green lines indicate the assumed source position for the response simulations and the region from which the spectra are extracted, respectively. Events below 5 keV are also included in this image for emphasizing the noisy strips.

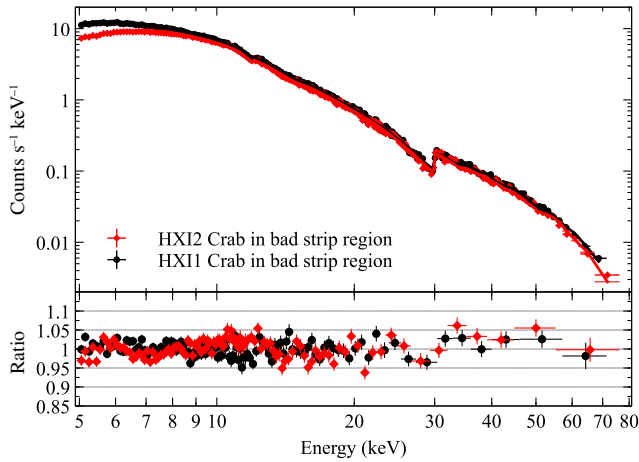


**Fig. 10** Crab spectra extracted from a  $20'' \times 540''$  rectangular region covering the noisy strips, and the ratio between the spectra and an absorbed broken-powerlaw model.

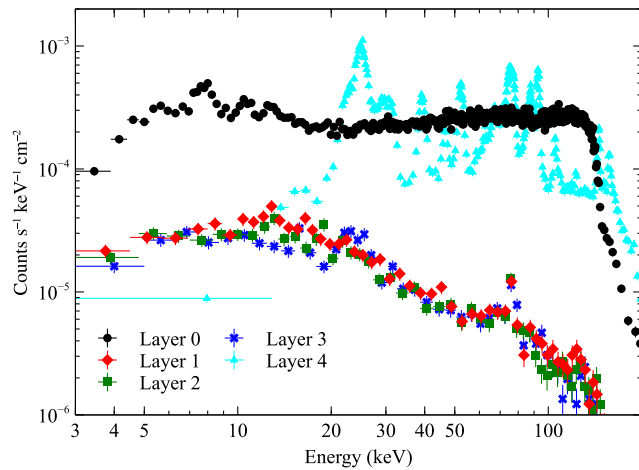


**Fig. 11** HXI2 NXB spectra extracted from Earth occultation data. The spectra are extracted from whole detector area and scaled with its geometrical area. Note that a cutoff at  $\sim 120$  keV in DSSDs is due to the upper limit of the dynamic range of slow shapers in read-out ASICs, while that at  $\sim 150$  keV in CdTe-DSD is due to the upper limit of the ADC in ASICs.

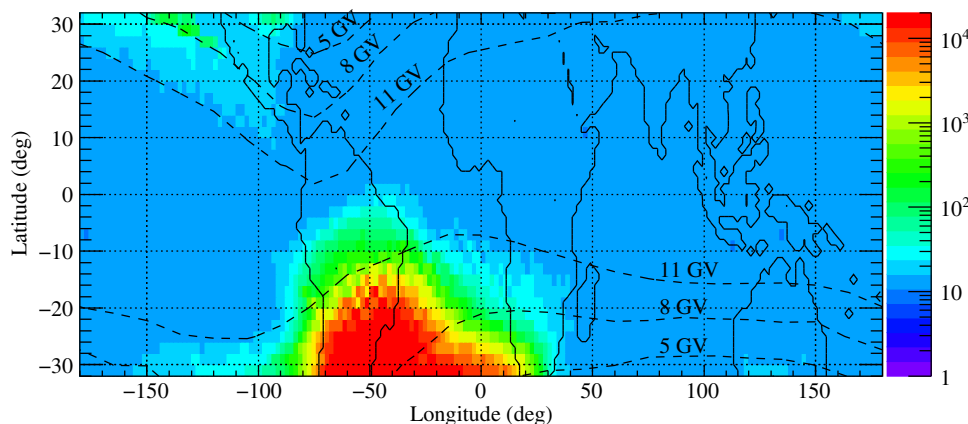


**Fig. 12** Distribution of trigger rate of the HXI2 top-layer DSSD during Earth occultation and blank sky observations. Black dashed lines indicate the geomagnetic cutoff rigidity.

The difference cannot be explained if it is caused by  $\sim 100$  keV photons. It means that this background component originates from particles with low penetrating power. The second reason is the distribution of the background rate. Figure 12 shows a trigger rate of the HXI2 top-layer DSSD as a function of latitude and longitude of the satellite. It extends larger than the SAA and has a hot region at above North America. The hot region does not simply depend on the geomagnetic cutoff rigidity because it is not seen in other regions. This distribution is consistent with the electron distribution ( $>93$  keV) observed by DEMETER/IDP in orbit.<sup>40</sup>

NuSTAR might observe this electron background as well. According to a web page on the background filtering,<sup>41</sup> a “tentacle”-like region of higher activity is found to be located around  $\sim -90^\circ$  longitude and above about  $-2^\circ$  latitude. This region is consistent with the distribution of the low-energy electrons as shown in Figs. 12 and 14.

The albedo electrons cannot directly come into the HXI imager because baffles made of Pb/Sn shields are implemented to block the stray light and CXB out of the FoV. Thus, top-layer DSSD probably suffers from the electrons scattering on the HXI-S entrance window (two layers of  $30\text{-}\mu\text{m}$ -thick poly-carbonate sheets) or the extensible optical bench. To reduce this background, we should have baffled the entrance window from the low-energy albedo electrons.

Since the electron background strongly depends on the satellite position as shown in Fig. 12, a selection with the satellite position successfully reduces top-layer DSSD background down to 10% to 20% level as shown in Fig. 13. The definition of the regions discarded in this selection is shown in red lines in Fig. 14. This region is implemented in the standard screening procedure as `SAA2_HXI`. This selection reduces observation efficiency as well. Area of the selected regions (which excludes the SAA as well) is  $\approx 67\%$  of the total area where the satellite orbits above, while those of Suzaku SAA definition is  $\approx 88\%$ .

The electron background depends on the satellite position, even after excluding the high background regions using the satellite position selection. Figure 14 shows a distribution of count rate of HXI2 top-layer DSSD with  $PI > 800$  corresponding to  $E > 80.0$  keV, which should have only background events. Clearly, the background level in top-layer DSSD is lower at  $-50^\circ \lesssim \text{lat} \lesssim 100^\circ$  and  $\text{lon} \gtrsim 0^\circ$ , while it is higher at  $-150^\circ \lesssim \text{lat} \lesssim -100^\circ$ . To investigate the position dependence of the top-layer DSSD background, spectra are extracted from six

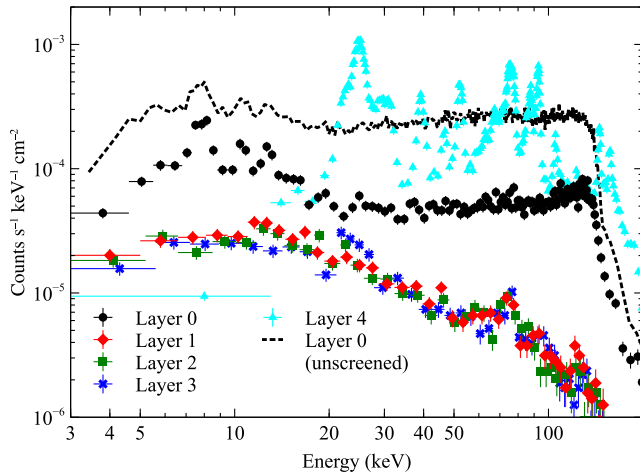


**Fig. 13** HXI2 NXB spectra screened with satellite position. Unscreened NXB spectrum of layer 0 (top-layer DSSD), which is already shown in Fig. 11, is also overlotted as a comparison.

regions, which are divided at  $\text{lon} = -60^\circ, 60^\circ$  and  $\text{lat} = 0^\circ$ . In Fig. 15, spectra from regions with highest and lowest background levels are plotted. Although there is a large difference at higher energies, it does not affect the scientific analysis because signals above 30 keV in top-layer DSSDs are discarded in the energy-dependent layer selection. At energies below 30 keV, the background level can change by a factor of 3 at maximum depending on the orbital phase.

## 5.2 Properties of CdTe-DSD Background

NXB in the CdTe-DSD (layer 4) of HXI is composed of many activation lines from radioactive isotopes induced by geomagnetically trapped protons in the SAA as shown in the cyan histogram in Fig. 13. Since orbit inclination angle of Hitomi is 31 deg, the HXI passes the SAA for 8 to 9 times a day. Low-energy protons trapped in the SAA generate radioactive isotopes inside the detectors via interactions between protons and heavy atoms, such as Cd, Te, and Bi, contained in the CdTe-DSSDs and BGO shields. Gamma-ray photons and  $\beta$  particles from these radioactive isotopes are the main cause of the CdTe-DSD background.

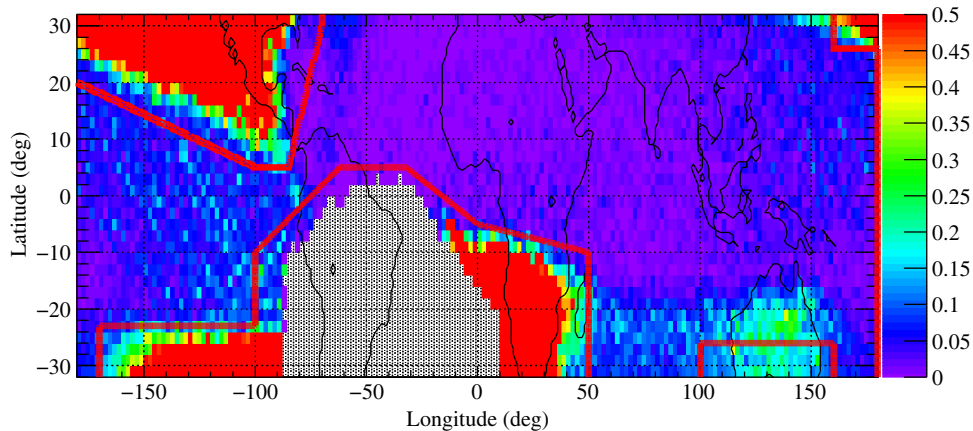


**Fig. 14** Distribution of count rate of the HXI2 top-layer DSSD with  $\text{PI} > 800$  during Earth occultation and blank sky observations. Signals in regions enclosed by red lines are ignored by the satellite position selection.

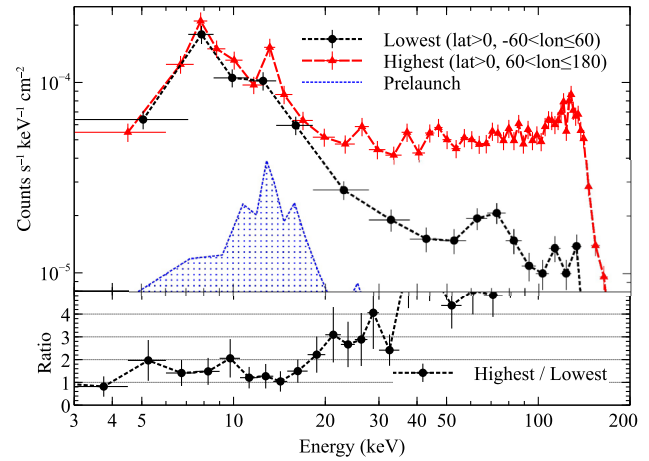


**Fig. 15** HXI2 NXB spectra of top-layer DSSD extracted from high and low background regions, after the final screening.

Since the radioactive isotopes are generated in the SAA passage, the CdTe-DSD background depends on the time after the SAA passage, which is defined as  $T_{\text{SAA}}$ . Figure 16 shows spectra sorted by  $T_{\text{SAA}}$ . In this figure, the SAA pass is defined as  $T_{\text{SAA}} < 5000$ , where 5000 s roughly corresponds to one orbital period of Hitomi, and non-SAA pass is defined as  $T_{\text{SAA}} > 6000$ . It is clear that a few lines at  $\approx 25$  keV and  $\approx 160$  keV are rapidly decaying after the SAA passage, but spectra at 30 to 80 keV, which are used for scientific analysis, show less variability  $\lesssim 30\%$ .

The properties of activation background in the CdTe-DSD observed by the HXI give us essential information to understand the activation background and significantly improved the accuracy of the simulations of the activation background. Details of the simulation studies are described by Odaoka.<sup>42</sup> This result will be a great help for future hard x-ray missions, such as FORCE.<sup>43</sup>

## 5.3 Final Background Spectra

The final spectrum of the NXB and blank sky after all the processing and screening is shown Fig. 17. Compared with the NXB spectra before the energy-dependent layer selection (Fig. 13), the total background level is clearly reduced by

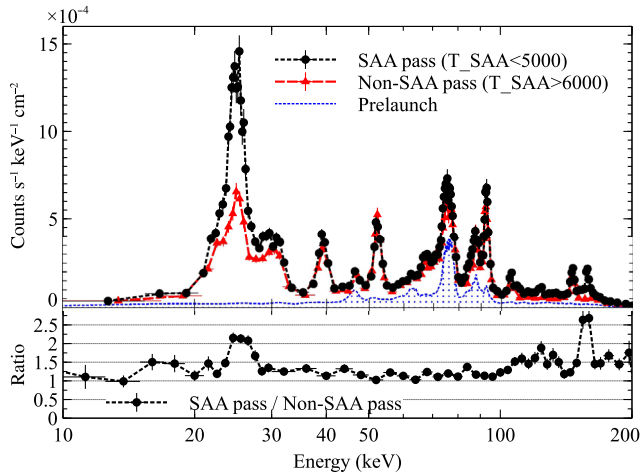


**Fig. 16** HXI2 NXB spectra of CdTe-DSD sorted with  $T\_SAA$ . Lines at 46 and 63 keV in prelaunch data are thought to be intrinsic lines. The lines at 70 to 80 keV are Bi-K lines from the BGO shield.

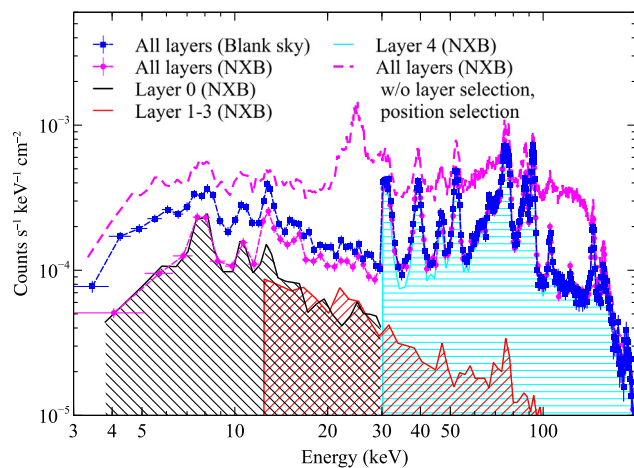


**Fig. 17** The final spectrum of HXI2 NXB and blank sky. The spectra in layer 0, layers 1 to 3, and layer 4 of HXI2 NXB after the energy-dependent layer selection are shown as shaded regions.

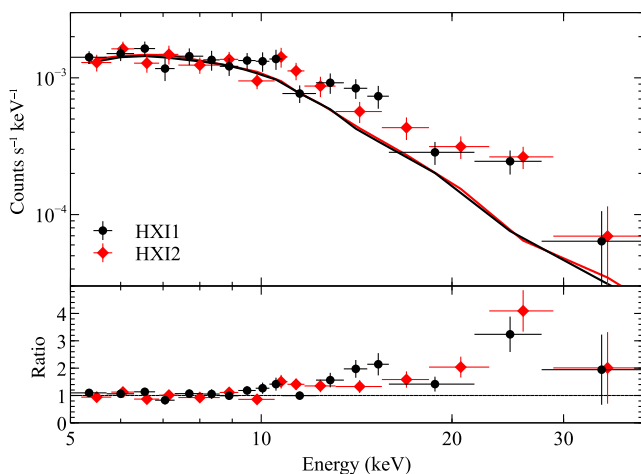


**Fig. 18** The CXB spectra observed by the HXI (black/red points) compared with the historically measured CXB spectral model<sup>44</sup> (black/red solid curves).

ignoring the strong line at 20 to 30 keV in CdTe-DSD and the albedo electron component dominating the higher energy region in top-layer DSSD. The NXB level is as low as the preflight requirement of  $1 - 3 \times 10^{-4}$  counts  $s^{-1} cm^{-2} keV^{-1}$ . The photon detection efficiency of the top-layer DSSD above 30 keV is ignorable, while that of the four layers of DSSDs (in total 2-mm thick) below 30 keV is  $\gtrsim 50\%$ . Therefore, the energy-dependent layer selection efficiently reduces the background with a small loss of detection efficiency. It demonstrates the effectiveness of the design of the stacked semiconductor detector for achieving better sensitivity.

Figure 17 shows one additional demonstration of the HXI performance. A clear spectral difference between the blank sky and NXB spectra can be seen below  $\approx 30$  keV. It indicates that the HXI is able to detect the CXB below  $\approx 30$  keV. Indeed, as shown in Fig. 18, the CXB spectra are significantly detected by the HXI. In this figure, a powerlaw model with a photon index of  $\Gamma = 1.41$  is overlotted as a historically measured spectral model of the CXB.<sup>44</sup> Spectral fitting by this model with a fixed photon index provides the best-fit powerlaw normalization at 1 keV of  $(9.0 \pm 0.5) \times 10^{-5}$   $cm^{-2} photons^{-1} keV^{-1}$ . Here, the spectral fitting is performed in 5 to 10 keV because the 15- to 30-keV spectra deviate from the powerlaw model due to the variability of the albedo electron background as previously shown in Fig. 15. If the accuracy of background modeling is improved, it would be possible to detect the CXB spectra above 30 keV. A ratio of the best-fit normalization with the value reported by De Luca and Molendi<sup>44</sup> is  $1.13 \pm 0.06$ , which is roughly consistent with the CXB fluctuation,  $\sigma_{CXB}/I_{CXB} \approx 13\%$  based on a relation of  $\sigma_{CXB}/I_{CXB} \propto \Omega_e^{-0.5} S_C^{-0.25}$ <sup>45</sup> with the HXI FoV  $\Omega_e = 0.023$   $deg^2$  and an assumed upper cutoff flux  $S_C = 8 \times 10^{-14}$   $erg s^{-1} cm^{-2}$ . Thus, this result shows that the HXI has a good sensitivity for extended sources, which enables detection of the CXB below 30 keV.

## 6 Conclusions

The HXI showed good performances and provided us important insights on the NXB in the hard x-ray band although it was lost after only two weeks of observations. The Crab spectra are well reproduced by the detector response constructed on the ground calibration data. The residual between the Crab spectra and the best-fit absorbed powerlaw model is less than  $\lesssim 5\%$  at energies below 50 keV. The best-fit spectral parameters of the Crab are consistent with the historically reported values. This result indicates the correctness of the telescope effective area of the HXT and the detector response of the HXI. The NXB in top-layer DSSD is found to be dominated by the background due to low-energy albedo electrons. Utilizing its strong dependence on the latitude and longitude, it can be reduced to 10% to 20%. Even after this selection, the electron background in 20- to 30-keV varies by a factor of 3, depending on the orbital phase. The activation background in the CdTe-DSDs above 30 keV is more stable within  $\lesssim 20\%$ . The final spectrum of the NXB after all the processing and screening satisfies the preflight requirement level of  $1 - 3 \times 10^{-4}$  counts  $s^{-1} cm^{-2} keV^{-1}$ , and it enables to detect the CXB. The properties of the in-orbit background of the HXI would be useful for the future hard x-ray missions.

## Acknowledgments

We acknowledge all the Hitomi team members, including many graduate students, for their great contributions to the HXI and

the Hitomi project. We acknowledge support from the JSPS/MEXT KAKENHI Grant Nos. 24105007, 15H03639, 25287059, and 24244014 and the JSPS Core-to-Core Program. All U.S. members acknowledge support through the NASA Science Mission Directorate. Stanford and SLAC members acknowledge support via DoE contract to SLAC National Accelerator Laboratory DE-AC3-76SF00515 and NASA Grant No. NNX15AM19G. French members acknowledge support from the Centre National d'Etudes Spatiales.

## References

1. T. Takahashi et al., “The ASTRO-H x-ray astronomy satellite,” *J. Astron. Telesc. Instrum. Syst.* **4**(2), 021402 (2018).
2. K. Nakazawa et al., “The hard x-ray imager (HXI) onboard ASTRO-H,” *J. Astron. Telesc. Instrum. Syst.* **4**(2) (2018).
3. H. Matsumoto, H. Awaki, and A. Furuzawa, “In-orbit performance of the hard x-ray telescope (HXT) on board Hitomi,” *J. Astron. Telesc. Instrum. Syst.* **4**(1), 011212 (2018).
4. T. Takahashi et al., “Hard x-ray detector (HXD) on board Suzaku,” *Publ. Astron. Soc. Jpn.* **59**, S35–S51 (2007).
5. S. Watanabe et al., “Development of semiconductor imaging detectors for a Si/CdTe Compton camera,” *Nucl. Instrum. Methods Phys. Res., Sect. A* **579**, 871–877 (2007).
6. M. Kokubun et al., “Hard x-ray and gamma-ray detector for ASTRO-H based on Si and CdTe imaging sensors,” *Nucl. Instrum. Methods Phys. Res., Sect. A* **623**, 425–427 (2010).
7. H. Odaka et al., “High-resolution Compton cameras based on Si/CdTe double-sided strip detectors,” *Nucl. Instrum. Methods Phys. Res., Sect. A* **695**, 179–183 (2012).
8. G. Sato et al., “The Si/CdTe semiconductor camera of the ASTRO-H hard x-ray imager (HXI),” *Nucl. Instrum. Methods Phys. Res., Sect. A* **831**, 235–241 (2016).
9. S. Takeda et al., “Development of double-sided silicon strip detectors (DSSD) for a Compton telescope,” *Nucl. Instrum. Methods Phys. Res., Sect. A* **579**, 859–865 (2007).
10. K. Nakazawa et al., “A high-energy resolution 4cm-wide double-sided silicon strip detector,” *Nucl. Instrum. Methods Phys. Res., Sect. A* **573**, 44–47 (2007).
11. K. Hayashi et al., “Radiation effects on the silicon semiconductor detectors for the ASTRO-H mission,” *Nucl. Instrum. Methods Phys. Res., Sect. A* **699**, 225–229 (2013).
12. T. Takahashi, “Recent progress in CdTe and CdZnTe detectors,” *IEEE Trans. Nucl. Sci.* **48**(4), 950–959 (2001).
13. S. Ishikawa et al., “Performance of double-sided CdTe strip detectors for gamma-ray imaging and spectroscopy,” in *IEEE Nuclear Science Symp. Conf. Record (NSS '08)*, pp. 440–443, IEEE (2008).
14. S. Watanabe, S. Ishikawa, and H. Aono, “High energy resolution hard x-ray and gamma-ray imagers using CdTe diode devices,” *IEEE Trans. Nucl. Sci.* **56**(3), 777–782 (2009).
15. S. Ishikawa et al., “Development of double-sided CdTe strip detectors for  $\gamma$ -ray imaging and spectroscopy,” *Jpn. J. Appl. Phys.* **49**, 116702 (2010).
16. K. Hagino et al., “Imaging and spectral performance of CdTe double-sided strip detectors for the hard x-ray imager onboard ASTRO-H,” *Proc. SPIE* **8443**, 844355 (2012).
17. H. Tajima et al., “Performance of a low noise front-end ASIC for Si/CdTe detectors in Compton gamma-ray telescope,” *IEEE Trans. Nucl. Sci.* **51**, 842–847 (2004).
18. T. Saito et al., “Development of high performance avalanche photodiodes and dedicated analog systems for HXI/SGD detectors onboard the Astro-H mission,” *Nucl. Instrum. Methods Phys. Res., Sect. A* **699**, 230–234 (2013).
19. M. Ohno et al., “Development and verification of signal processing system of avalanche photo diode for the active shields onboard ASTRO-H,” *Nucl. Instrum. Methods Phys. Res., Sect. A* **831**, 410–414 (2016).
20. M. Ajello et al., “Cosmic x-ray background and earth albedo spectra with Swift BAT,” *Astrophys. J.* **689**, 666–677 (2008).
21. G. Bale et al., “Cooled CdZnTe detectors for x-ray astronomy,” *Nucl. Instrum. Methods Phys. Res., Sect. A* **436**(1), 150–154 (1999).
22. M. Lépy et al., “Experimental study of the response of semiconductor detectors to low-energy photons,” *Nucl. Instrum. Methods Phys. Res., Sect. A* **439**, 239–246 (2000).
23. M. Kokubun et al., “In-orbit performance of the hard x-ray detector on board Suzaku,” *Publ. Astron. Soc. Jpn.* **59**, S53–S76 (2007).
24. H. Odaka et al., “Development of an integrated response generator for Si/CdTe semiconductor Compton cameras,” *Nucl. Instrum. Methods Phys. Res., Sect. A* **624**, 303–309 (2010).
25. S. Agostinelli et al., “Geant4 simulation toolkit,” *Nucl. Instrum. Methods Phys. Res., Sect. A* **506**, 250–303 (2003).
26. J. Allison et al., “Geant4 developments and applications,” *IEEE Trans. Nucl. Sci.* **53**, 270–278 (2006).
27. M. Benoit and L. Hamel, “Simulation of charge collection processes in semiconductor CdZnTe  $\gamma$ -ray detectors,” *Nucl. Instrum. Methods Phys. Res., Sect. A* **606**, 508–516 (2009).
28. T. Kitaguchi et al., “Spectral calibration and modeling of the NuSTAR CdZnTe pixel detectors,” *Proc. SPIE* **8145**, 814507 (2011).
29. Z. He, “Review of the Shockley–Ramo theorem and its application in semiconductor gamma-ray detectors,” *Nucl. Instrum. Methods Phys. Res., Sect. A* **463**, 250–267 (2001).
30. K. Miyake et al., “Effects on hard x-ray response of a double-sided Si strip detector caused by interstrip surface charge,” *Proc. SPIE* **9968**, 99680D (2016).
31. S. Y. F. Chu, L. P. Ekstrom, and R. B. Firestone, “The Lund/LBNL nuclear data search,” Version 2.0, <http://nucldata.nuclear.lu.se/toi/> (February 1999).
32. M. Lépy, J. Plagnard, and L. Ferreux, “Measurement of  $^{241}\text{Am}$  L x-ray emission probabilities,” *Appl. Radiat. Isot.* **66**, 715–721 (2008).
33. K. A. Arnaud, “XSPEC: the first ten years,” in *Astronomical Data Analysis Software and Systems V*, Vol. 101, p. 17 (1996).
34. H. Mori et al., “On-ground calibration of the Hitomi hard x-ray telescopes,” *J. Astron. Telesc. Instrum. Syst.* **4**(1), 011210 (2018).
35. A. Toor and F. D. Seward, “The crab nebula as a calibration source for x-ray astronomy,” *Astron. J.* **79**, 995–999 (1974).
36. K. K. Madsen et al., “Measurement of the absolute crab flux with NuSTAR,” *Astrophys. J.* **841**, 56 (2017).
37. C. A. Wilson-Hodge et al., “When a standard candle flickers,” *Astrophys. J.* **727**, L40 (2011).
38. K. K. Madsen et al., “Broadband x-ray imaging and spectroscopy of the crab nebula and pulsar with NuSTAR,” *Astrophys. J.* **801**, 66 (2015).
39. T. Mizuno et al., “Monte Carlo simulation study of in-orbit background for the soft gamma-ray detector on-board ASTRO-H,” *Proc. SPIE* **7732**, 77323C (2010).
40. I. C. Whittaker et al., “Determining the spectra of radiation belt electron losses: fitting DEMETER electron flux observations for typical and storm times,” *J. Geophys. Res.: Space Phys.* **118**, 7611–7623 (2013).
41. “Background filtering | NuSTAR,” [www.nustar.caltech.edu/page/background](http://www.nustar.caltech.edu/page/background).
42. H. Odaka, “Modeling of proton-induced radioactivation background in hard x-ray telescopes: Geant4-based simulation and its verification by Hitomi’s measurement in a low earth orbit,” *Nucl. Instrum. Methods Phys. Res., Sect. A* **891**, 92–105 (2018).
43. K. Mori et al., “A broadband x-ray imaging spectroscopy with high-angular resolution: the FORCE mission,” *Proc. SPIE* **9905**, 99051O (2016).
44. A. De Luca and S. Molendi, “The 2–8 keV cosmic x-ray background spectrum as observed with XMM-Newton,” *Astron. Astrophys.* **419**, 837–848 (2004).
45. K. Nakazawa et al., “Hard x-ray properties of the merging cluster Abell 3667 as observed with Suzaku,” *Publ. Astron. Soc. Jpn.* **61**, 339–355 (2009).

**Kouichi Hagino** is an assistant professor at Tokyo University of Science. He received his BS and MS degrees in physics from the University of Tokyo in 2010 and 2012, respectively, and his PhD in physics from the University of Tokyo in 2015. He has been working on development of semiconductor detectors for high-energy astrophysics.

Biographies for the other authors are not available.